Proceedings of the ASME 2023
International Mechanical Engineering Congress and Exposition
IMECE2023
October 29 – November 2, 2013, New Orleans, LA, USA

IMECE2023-114379

USING ELECTRICAL RESISTANCE AS A DIAGNOSTIC DURING PROCESS-STRUCTURE-PROPERTY INVESTIGATION OF CNT FORESTS

Ramakrishna Surya[1], Filiz Bunyak[2], Prasad Calyam[2], Kannappan Palaniappan[2] Matthew R Maschmann[3]

[1] Department of Mechanical Engineering, University of Missouri, Columbia, MO
[2] Department of Electrical Engineering and Computer Science, University of Missouri, Columbia, MO
[3] MU Materials Science and Engineering Institute, University of Missouri, Columbia, MO

ABSTRACT

Controlling the self-assembly of carbon nanotube (CNT) forests is important for tailoring their ensemble properties for specific applications. In this study, real-time electrical resistance measurements of in-situ CNT forest syntheses was established as a method to interrogate the evolution of CNT forest morphology. The method employs in-situ scanning electron microscopy (SEM) synthesis techniques to correlate observed morphological changes to electrical resistance. A finite-element simulation was used to simulate CNT forest synthesis and the evolution of electrical resistance in a configuration like that used experimentally. The simulation considers the contribution of CNT electrical resistance, CNT-CNT junction resistance, and CNT-electrode contact resistance. Simulation results indicate that an increased number of CNT-CNT junctions with time have a diminishing effect on increasing electrical conductance. Experimentally observed increases in electrical resistance are attributed to increasing CNT delamination from the electrical contacts.

Keywords: carbon nanotube, in-situ, simulation

NOMENCLATURE

CNT	carbon nanotube
CVD	chemical vapor deposition
ESEM	environmental scanning electron microscope
MEMS	micro-electrical mechanical system
SEM	scanning electron microscope.
TEM	transmission electron microscope
SWNT	single-walled carbon nanotubes
MWCNT	multi-walled carbon nanotubes

1. INTRODUCTION

Carbon nanotubes possess exceptional engineering properties that surpass those of conventional materials, making them highly desirable for a range of applications such as multi-functional structural materials[1], [2], flexible sensors[3], [4], electronics[5], [6], and thermal interface materials[7], [8]. CNTs often occur as forests which are vertically aligned films with heights of several millimeters. The ensemble properties of CNT forests are significantly degraded when compared to the individual tubes due to various morphological features such as waviness kinks and inhomogeneities in density[3], [9]–[17]. Despite the role of these features in degrading the properties of CNT forests the mechanisms that govern their formation are only now being studied. Studies showing structure-mechanical properties have been done to obtain a rough correlation between mechanical properties and structure.

CNT forests are commonly produced through chemical vapor deposition techniques. A layer of a buffer material, typically alumina, is placed between the substrate and transition metal such as iron[18]. The substrate is then heated to a temperature between 600-800 °C. Traditionally, heating is done either by using a hot walled tube furnace or a cold walled tube furnace in the presence of H_2 gas a reducing agent and C_2H_2 or C_2H_4 acting as the carbon feedstock for CNT production. The mixture of hydrogen and feedstock gas is often delivered by an inert carrier gas such as Ar or He. In the reducing environment and at a high temperature the catalyst layer forms catalyst nanoparticles which then support the growth of carbon nanotubes.

In-situ transmission electron microscope (TEM) synthesis techniques have directly observed the synthesis of CNTs and small CNT populations[19]–[23]. These techniques use cold-walled CVD methods for CNT synthesis within the TEM chamber. Heat is supplied by a thin film heating element

embedded in a silicon microchip. Gas is delivered to the chip either by direct vapor delivery within the TEM chamber (environmental TEM), or by enclosing the gas in a sealed membrane[24]. Image acquisition rates typically exceed 1,000 frames per second, enabling dynamic image sequences. TEM's imaging resolution allows for the direct imaging of individual CNTs during growth instead of population-averaged measurements. In-situ TEM techniques also enable researchers to examine catalyst nanoparticles with atomic precision to identify parameters that facilitate catalytic activity. Recent studies have used in-situ TEM to examine the nucleation, self-assembly, and early growth of CNT forests, observing the mechanical competition between contacting CNTs lengthening at different rates[22]. The reaction forces generated were sufficient to kink multiwalled CNTs. However, the limited depth of field and field width restrict the scope of observation. Additionally, because image acquisition in TEM is via transmission through a sample, height-resolved characterization is difficult as the resulting image represents a projection through the height of a CNT forest.

Electrical resistance of CNTs is based on several factors such as diameter, density, and lattice structure. Depending on the combination of these properties the CNT can either exhibit a metallic or non-metallic/semi-conductor behavior[25]. Since the growth of a nanotube is in any process is a random phenomenon, it is assumed that all combinations are possible. Statistically, one third of the CNTs that form would exhibit metallic behavior while the remaining two thirds would behave like a semi-conductor. The conductivity range of CNT forests obtained by experimentation is quite large i.e., $8 \times 10^{-6} – 20 \times 10^{-6}$ Ω-m. CNTs are characterized by their large current carrying capacities with current densities as high as 10^{13}A/cm2 in the case of SWNTs and values of $>10^{9}$A/cm2 in the case of MWCNTs[26]. Prior studies have been done to study the electrical properties of CNTs when added to a polymer. CNTs, owing to their size and morphology lead to very high aspect ratios that make it possible to reach electrical conductivity values at very low concentrations, which affects the polymer density[27]. Global electrical conductivity of CNTs is based on the formation of electrically conductive paths between CNTs through a three-dimensional network created internally. Therefore, the conductivity is not just based on a single CNT but on a series of CNTs and CNT-CNT contacts. The amount of CNTs needed to create a conductive pathway is known as a percolation threshold and has been extensively studied for different systems. Alternatively, percolation threshold can be defined as the minimum volume fraction of the CNTs necessary to create an electrical network that allows an effective current flow through the material[28].

In composites it is not necessary that there is direct contact between the CNTs since tunneling effect may occur between neighboring CNTs when they are in proximity. The maximum value of the tunneling distances observed in neighboring CNTs was 10nm. The equation that governs the electrical conductivity of conductive nanoparticles such as CNTs which are added to polymer matrices is based on employment of power law, which is based on conventional percolation theory:

$$\sigma = \sigma_0(\varphi - \varphi_0)^t$$

where σ is the electrical conductivity, σ0 is the pre-exponential factor, φ is the volume fraction of CNTs in the nanocomposite, φ_0 is the volume fraction at the percolation threshold, t is determined experimentally and is called the critical conductivity exponent. The value of t typically ranges between 1.3-2 for CNT films, coatings, and bulk composites respectively. Percolation threshold is typically expressed as a function of geometric parameters of the CNTs and is calculated upon the assumption that the CNT are uniformly and randomly distributed in the hosting media. The formula that governs the percolation threshold is as follows:

$$\phi_p = \frac{D}{2L}$$

where ϕ_p stands for percolation threshold, D the CNT diameter and L is the length of the CNT where L/D>>1[29].

To navigate the high-dimensional synthesis space of CNT forests researchers have developed a high-throughput, autonomous research robot which can deterministically synthesize isolated SWNTs. The Autonomous Research Systems (ARES) uses Raman spectroscopy to characterize growing CNTs in-situ. The ARES system utilizes the principles of machine learning (ML) to learn from previous results and uses a planner powered by artificial intelligence (AI) to schedule experiments and obtain experimental objectives[30]. The ARES approach demonstrates that integrating ML and AI with high throughput experimentation can facilitate experimental parameter space navigation which was previously not possible[31].

Physical experimental results are supplemented with a time-resolved finite element method (FEM) CNT forest simulation which is used as a high-throughput virtual laboratory. In previous work, the simulation in tandem with CNTNet; a custom deep neural network and a property regression module; was used to predict mechanical properties of CNT forests and was able to classify synthetic CNT[32]–[34] forest image-based parameters such as density, radius, and standard deviation of growth rate with an accuracy of 91%[35]. For this study the simulation is modified to measure the electrical properties of CNT forests. Not only would this increase the throughput of the electrothermal experimentation, but also add another facet into the synthesis-structure-property design loop helping achieve more control over the final properties of CNT forests.

2. MATERIALS AND METHODS

For all experiments, a Protochips Fusion 350 stage and an FEI Quanta 600F environmental scanning electron microscope (ESEM) were used. The stage was fastened to the SEM stage with a set screw, and each experiment was performed using a MEMS-based heating and electrical biasing chip known as an E-chip. The E-chips used had a SiC thin film heating element, which enabled uniform heating of an area up to 300 x 300 μm. A schematic of a heating chip is shown in Figure 2 with an inset

showing the heated zone. The heating area comprises a 3 x 3 array of holes. Apart from the electrodes that are used to heat the chip surface there are two pairs of tungsten electrodes between the main leads that are used to apply either a current or a voltage bias enabling real-time electrical property measurements. The surface of the chip is coated in silicon nitride and the electrodes are made of tungsten. Spring-loaded contact arms established electrical contact between the heating chip and the stage, and the Protochips Clarity control software, with the aid of an external computer, regulated the heating rate and setpoint temperature. The SEM control software captured time sequences of SEM images.

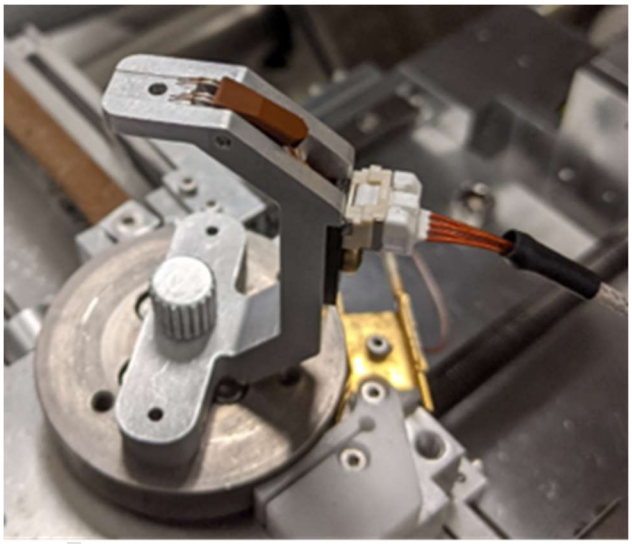

Figure 1. Protochips SEM stage with attached four channel cable installed within a FEI quanta environmental SEM chamber.

To deposit thin film catalyst layers on the E-chips, sputtering was performed at a base pressure of 1 x 10^{-7} Torr using a SouthBay Technology ion beam sputtering system. The system deposited 12 nm of alumina and 2 nm of iron, using a crystalline sapphire target as an alumina target and a 99.99% pure iron target as a source of iron. The alumina layer acts as a diffusion barrier layer, while the iron layer serves as the active catalyst. Before deposition, the iron target was cleaned with an ion beam to eliminate possible surface oxidation and contamination, and the catalyst thickness was monitored using a quartz crystal microbalance.

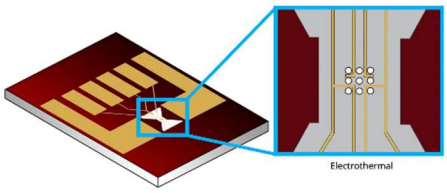

Figure 2. Schematic of a Protochips fusion electrothermal e-chip. the inset shows a magnified representation of the heated region along with electrodes[36].

Acetylene gas was introduced to the SEM chamber. In conventional CNT forest synthesis experiments conducted at atmospheric pressure, an inert carrier gas (Ar, He) and hydrogen are often employed in addition to a hydrocarbon gas like acetylene. Recent in-situ TEM experiments have shown that hydrogen is ineffective at reducing oxidized iron at the pressures typical of electron microscopes[20]. Therefore, in this study, the hydrogen gas was replaced with acetylene which was passed through a desiccant gas drier to eliminate residual water vapor, and a cold trap was affixed to the SEM chamber to condense water vapor contaminants and decrease the SEM base pressure. To route acetylene from the gas cylinder to the SEM chamber, stainless steel tubing was used, and a pressure limiting aperture was employed to enhance image resolution in the gaseous environment. The cold trap is baked at 90 °C for 4-5 hours prior to the experiment to prevent any surface degassing when placed in the SEM.

To decrease the surface energy of the heating chips and minimize the migration of iron nanoparticles during high-temperature processing, plasma passivation was performed using a PELCO easiGlow glow discharge cleaning system. The treatment of the chips was performed at a base pressure of 0.2 Torr for a duration of 300 seconds (about 5 minutes) with a current of 10 μA.

The SEM stage and chip were installed, followed by high vacuum pumping for 16 hours (overnight). Acetylene gas was then purged into the SEM chamber, at a maximum pressure of 150 Pa, and the acetylene pressure was maintained by the FEI SEM software interface during the experiments. Previously, liquid nitrogen was used as the coolant in the cold trap, after several experiments it was observed that when the SEM chamber was filled with acetylene for the experiment a portion of it would condense onto the cold trap causing a 'acetylene sink' which would hinder the experiment. To mitigate this a slurry of acetone and dry ice was used. Prior to introducing acetylene, the base vacuum level in the chamber reached between 3 x 10^{-4} – 9 x 10^{-4} Pa (2.25 x 10-6 – 6.75 x 10-6 Torr). Typical imaging parameters included an acceleration voltage of 5 kV and a spot size of 3.5, while the typical working distance was 8 mm. Image focus and stigmation were first tuned in high vacuum [37].

The SEM chamber was filled with acetylene gas at a pressure of 15 Pa. The pressure was allowed to stabilize before turning on the electron beam, and the imaging conditions were adjusted accordingly to fit the gaseous environment. The heating chips were gradually heated at a rate of 15 °C per second, utilizing closed-loop temperature control while applying a biasing voltage of 1V. Although there was some evidence of thermal drift in the chip, no active image compensation was attempted during the heating stage. Once the final synthesis temperature was achieved, the images were acquired at a rate of 30 frames/minute. The stage translation and image magnification are adjusted during the process.

The simulated synthesis of carbon nanotube forests was conducted using 3-dimensional finite element code developed in MATLAB. The simulation was analogous to our previously reported two-dimensional simulation[33]–[35], with the stiffness

matrix adjusted to accommodate the third dimension. In brief, a field of carbon nanotubes was established within the simulation domain, and the length of each carbon nanotube was incremented by its growth rate as the simulation looped iteratively through time. The CNTs were assigned a growth rate randomly based upon a gaussian distribution of growth rates. The CNT density was varied between 1-3 x 10^{10} CNT/cm^2[23]. The mean growth rate was 60 nanometers per time interval, with a population variance of 7%. The outer diameter of all CNTs was 10 nm, with an inner diameter of 5 nm. CNTs interacted with each other we are simulated van der Waals forces, approximated as linear elastic stiffness elements in the simulation. As the discrete time steps increment, the population of CNTs is allowed to interact and the form in response to CNT-CNT interactions. Mechanical equilibrium is computed for each discrete time step.

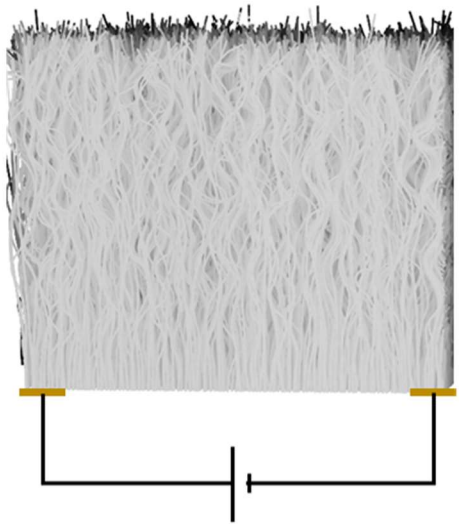

Figure 2. Schematic of finite element simulation configuration.

The simulation domain was 12 µm in width, 2 µm in width in depth, and approximately 12 µm in width of CNT forest height. The initial and final 1 µm in length was assumed to reside on the positive and negative electrodes (Figure 2). Electrical bias (1V) was applied across the width of the simulation domain to emulate the physical experiments. The CNT-CNT junction resistance was assumed to be 50,000 ohms. Further, the contact resistance between CNT and electrodes was assumed to be 10,000 ohms. The inherent conductivity of each CNT element (average length = 60 nm) was assumed to be 1 S, such that the overall conductivity of the CNT forest was governed by CNT-CNT contacts and CNT-electrode contact resistance. The resulting current flow from the interconnected carbon nanotube forest was measured once a fully interconnected electrical pathway was established. The resulting electrical resistance was obtained by dividing the bias voltage by the resulting current. electrical conductivity is the inverse of electrical resistance.

3. RESULTS AND DISCUSSION

3.1 CNT synthesis

The initial stage of synthesizing a CNT forest involves reducing the iron catalyst film through a chemical process that occurs at or close to the synthesis temperature of 625 °C. This reduction is followed by de-wetting of the film, which results in the formation of discrete nanoparticles. During atmospheric pressure CVD synthesis, this reduction and evolution of catalyst particles typically takes place in a hydrogen environment that is diluted with a carrier gas such as helium or argon. However, when operating at relatively low pressures such as ones found in electron microscopes, hydrogen loses its efficacy to reduce the catalyst film within the typical timeframe of atmospheric CVD syntheses. In TEM studies, it was observed that catalyst nanoparticle formation also occurs in the presence of acetylene[20]–[22].

Trace amounts of carbon aids with iron nanoparticle reduction, and thus a layer of adventitious carbon was deposited on the substrate using the electron beam. A 13 µm x 13 µm square of carbon was deposited between the biasing electrodes using an extended electron beam dwelt time. Care was taken to keep the carbon deposition constrained between the electrodes with an overlap of approximately 1µm[38].

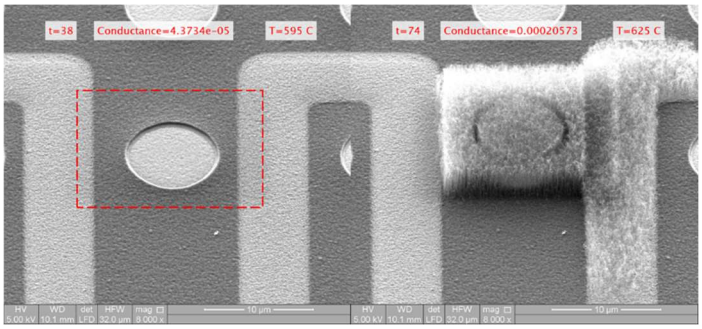

Figure 3. In situ SEM synthesis of CNT forest micropillar (right) on a predefined patch of carbon defined by the initial scan area (shown in red).

3.2 CNT Forest Density vs Resistance

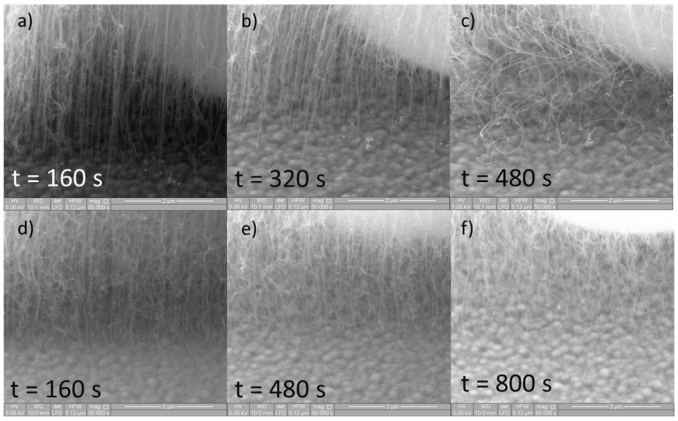

Figure 4: In-situ SEM synthesis image frames. Experiment #1 shown in a, b, c and experiment #2 showing in d, e, f. Time progresses from left to right in each image sequence. Both experiments exhibit delamination of CNTs as evident by the decrease in CNTs. All images were captured at a temperature of 625ºC.

The conductance values during the initial temperature ramp are very low. The conductance vs. time for two experiments is shown in Figure 5. During the initial phase of the synthesis experiments, the iron catalyst film is in an oxidized state, and resistance between the two lateral electrodes is high. There is an observable increase in conductance as temperature approaches 500 ºC due to iron oxide (catalyst) reduction. This trend of increasing conductivity is seen after CNTs start forming at approximately 600 ºC. This can be attributed to an increase in CNT-CNT contacts as growing CNTs interact. In both the experiments it is observed that the conductance values increases, peak, and then declines with increase in time. The plateau occurs well after the initiation of CNT forest synthesis.

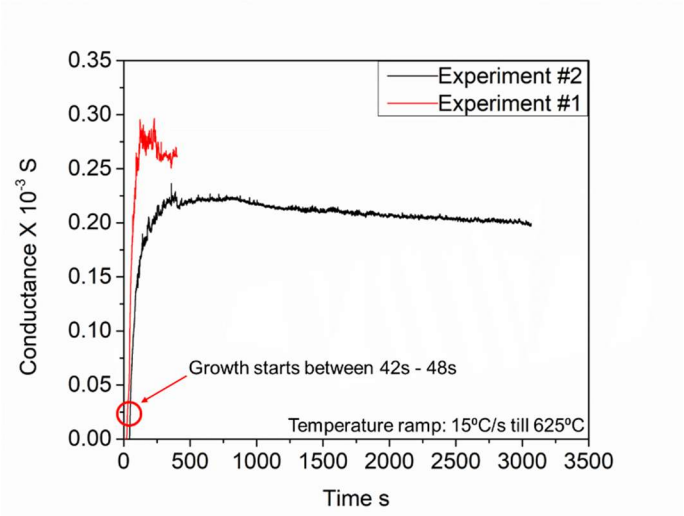

Figure 5: Experimentally observed conductance for two in-situ SEM synthesis experiments. The experiments were conducted using identical processing and synthesis conditions.

The plateau in electrical conductance represents the competition of two phenomena. The cooperative electrical transport between CNT-CNT contacts increases with time if a CNT forest grows. This mechanism increases the conductance across a CNT forest. However, CNT delamination from the growth substrate has a negative influence on the electrical conductivity. As CNTs are removed from the biasing electrodes, the number of conductive pathways is reduced. The number of CNT contacts with the electrodes are orders of magnitude lower than the internal CNT-CNT junctions, such that the gradual loss of even few CNTs from the electrode will produce an outsized influence on electrical conductance.

The reduction in CNT density with time can be observed in SEM images obtained during the in-situ experiment (Figure 4). This reduction in density is caused by delamination of CNTs from the growth substrate. Image sequences illustrated in Figure 4 (a-c) and (d-f) demonstrate the CNT density decay over time. In experiment #1 the total growth duration is 280 seconds. Experiment #2, which used identical synthesis and processing conditions, exhibited growth for > 3000 seconds. In this experiment, the electrical conductivity peaked at approximately 2.2 x 10^{-4} S after approximately 300 seconds of synthesis time. The conductance was relatively constant between 300 – 700 seconds. Conductance then decreased for the remainder of the synthesis time. The rate of conductance decrease was nearly constant from 700 – 3200 seconds.

A CNT areal density was computed by dividing the quantity of CNTs by the SEM observation area. The horizontal field width of each image was 5.12 µm. While the depth of field in the SEM images in not known precisely, we estimated a depth of field of 2.6 µm. The representative CNT forest densities computed by this method is shown in Figure 6 for two experiments. In both experiments, the number density was on the order of 10^{10} CNT/cm^2, consistent with SAXS measurement obtained by others shortly after the onset of CNT forest growth[23]. The density rapidly decreased throughout the observation duration. Note that the density observation period begins after the onset of CNT forest growth to accommodate for image focusing.

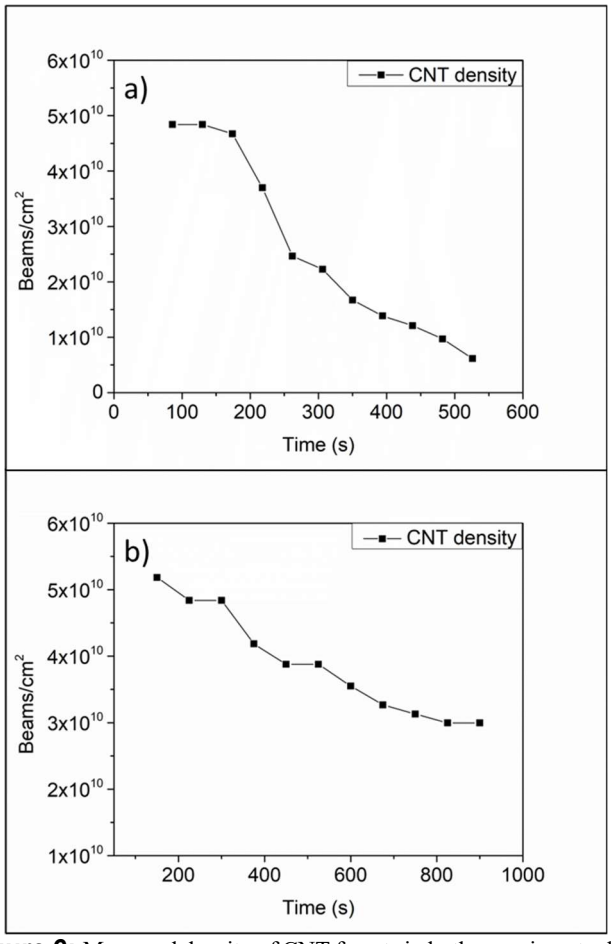

Figure 6: Measured density of CNT forests in both experiments show a reduction over time caused by delamination.

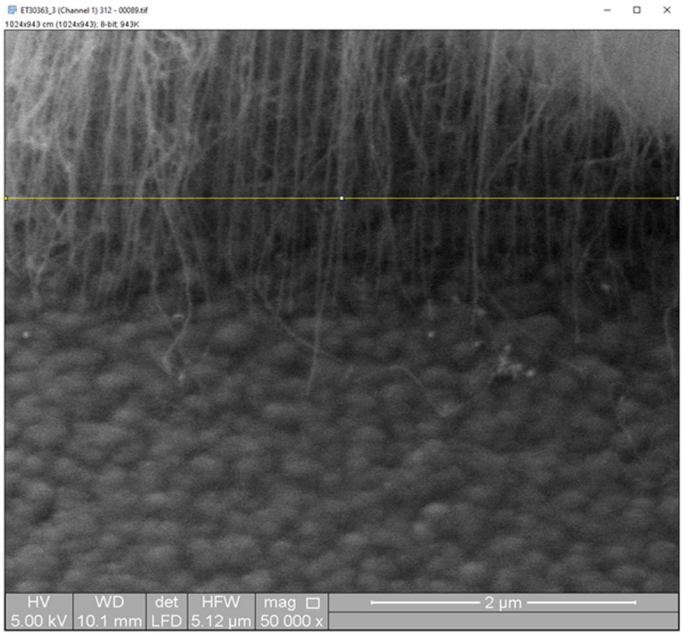

Figure 7: CNT density measurements using pixel grayscale intensity, as measured by Fiji's ImageJ. CNT forest SEM image with row of interest[39].

CNT density was estimated using the Fiji distribution of ImageJ[39]. A row from the CNT growth image sequence is taken and shown in Figure 7a and the pixel intensities are plotted where the peaks represent the CNTs in the foreground. Due to the temporal nature of the in-situ growth image sequence there is some inherent noise in the images which causes several spurious peaks which can be removed by smoothing the image. Not only does smoothing the image help with reducing the noise, but it also reduces the number of backgrounds CNTs being marked as foreground CNTs which makes the density calculation more accurate. Local peak maxima are calculated using the in-built tools in ImageJ. These peaks are then counted as the number of CNTs in plane of vision which adjusted accordingly to obtain density of CNTs per square centimeter.

3.3 Simulation

The simulation assumed an ideal situation in which all CNTs remained on the substrate throughout the simulation. The number of CNT-CNT junctions were a strong function of growth time and the areal density of CNTs within the forest, shown in Figure 8a. CNT-CNT contacts formed in the first few time steps and accumulate at a nearly constant rate through the simulation duration. At the last time step of the simulation, the total number of CNT-CNT contacts for 1, 2, and $3x10^{10}$ CNT/cm^2 was 791,630, 1,749,600, 3,396,400, respectively.

Because the CNTs themselves are quite conductive, the electrical conductance across the CNT forest is expected to be largely associated with charge transport between CNT-CNT contacts. The CNT Forest conductance is plotted as a function of simulation time steps (Figure 8b) and the number of CNT-CNT contacts (Figure 8c) for the 3 CNT forest densities. In the simulations, electrical conductance is measured only when a continuous pathway between the two electrodes is established. The conductive pathway was established at time steps 230, 90, and 38, for CNT forest densities of 1, 2, and $3x10^{10}$ CNT/cm^2, respectively. The time required to form a continuous electrical pathway, therefore, decreases with an increase in the CNT forest areal density, as expected. The conductance increases with time for all densities, reflecting the increase in CNT-CNT contacts that also increase with time. This behavior is reflected in the early stages of experiments shown in Figure 5.

With the simulation, the conductance can also be directly related to the quantity of CNT-CNT contacts. For all densities, the conductance increases as a function of CNT-CNT contact density. Interestingly, the lowest density CNT forest exhibits the highest conductance as a function of CNT-CNT contacts. We attribute this result to the fact that the electrical current must pass through fewer contacts in low-density forests to bridge the two electrodes. The highest-density forest consistently exhibited the lowest conductivity as a function of CNT contacts.

Because the simulation did not capture delamination events, it was unable to capture the effect of diminishing CNT density. The experimental results show a decreased CNT forest density with time as CNTs are delaminated from the growth substrate. As CNTs delaminate from the electrodes, the number of conductive pathways decrease. Because the number of CNT-electrode contacts is anticipated to be significantly fewer than the quantity of CNT-CNT contacts, the sensitivity of conductivity to the quantity of CNT-electrodes is expected to be significantly greater.

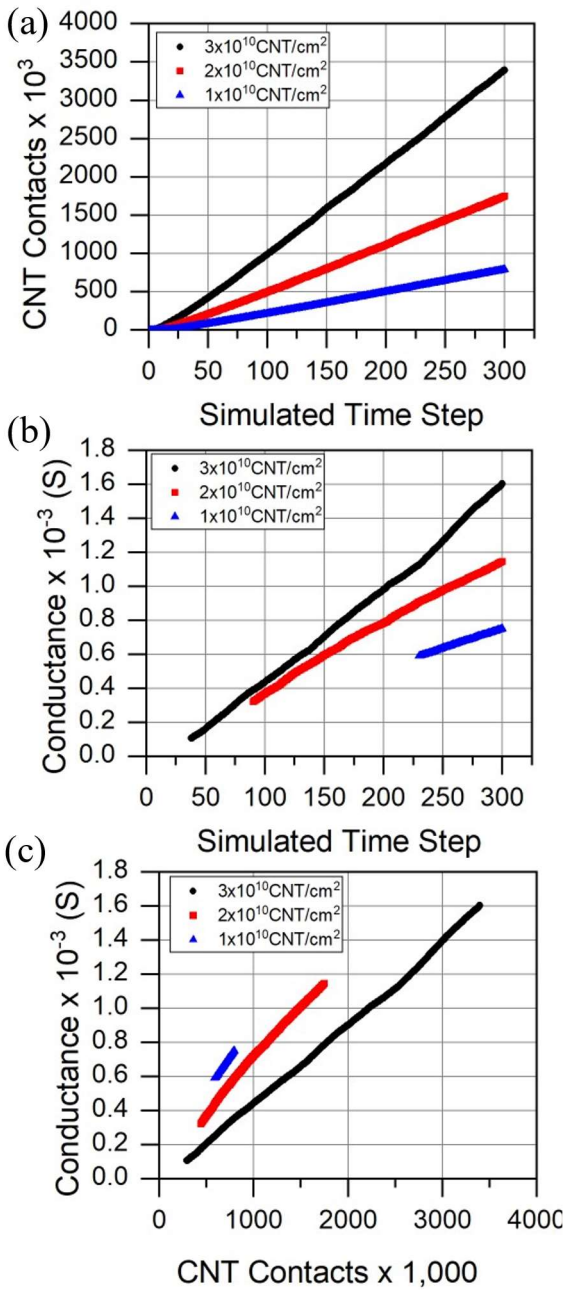

Figure 8: Finite element simulation output for simulation of 2 and 3 x 10^{10} CNT/cm^2 CNT forest syntheses. (a) The number of CNT-CNT contacts established as a function of simulation time step. (b) The lateral conductance of CNT forests as a function of time step. (c) The lateral conductance as a function of the quantity of CNT contact points.

3.4 Perspective

The preliminary results represent initial experiments in which electrical conduction was used as a diagnostic tool for CNT morphological development. The experiments demonstrate that the technique is sensitive to the changing morphology of growing CNT forests. Additional work is needed to enhance the uniformity of CNT forest synthesis on the measurement electrodes to match that observed between the electrodes. Likewise, CNT delamination will be added to the finite element code to simulate the detachment of CNTs from the measurement electrodes during synthesis. Once synthesis uniformity is obtained and delamination is incorporated into the simulation, the correlation between experiments and simulation will provide insights into the mechanisms responsible for the changes in electrical conductivity as CNT forest morphology evolves.

4. CONCLUSION

We have demonstrated application of in-situ electrical resistance as a methodology to characterize the evolving morphology of actively growing CNT forests. In-situ SEM synthesis allowed us to correlate initial findings with likely mechanisms. Increased conductance during the early phases of CNT forest synthesis are correlated to a rapid increase in CNT-CNT contacts. A decrease in conductance during later phases of synthesis are correlated to CNT delamination from the biasing electrodes. The magnitude of delamination was measured directly from in-situ SEM images.

Nonuniformity in the CNT synthesis on the biasing electrodes hindered the direct correlation of CNT forest density to electrical conductance. We are actively pursuing methods to increase the synthesis uniformity such that the relative contributions between CNT-CNT contact and CNT-electrode contacts may be more firmly established.

Finite element simulation of the synthesis process demonstrated that the quantity of CNT-CNT contacts is nearly linearly related to an increase in electrical conductance. However, the simulation was not capable of capturing the effects of CNT delamination. As a result, the full lifecycle of the CNT forest could not be captured. As the physical and numerical tools are matured, we hope to use electrical conductance as a metric to dynamically assess the evolving morphology of CNT forests as related to CNT-CNT contact density, CNT areal density, and CNT delamination vs. time.

ACKNOWLEDGEMENTS

All authors acknowledge the National Science Foundation grant #2026847 for funding. Authors acknowledge electron microscopy support from Dr. Dave Stalla from the MU Electron Microscopy Core.

REFERENCES.

[1] S. S. Wicks, R. G. de Villoria, and B. L. Wardle, ‘Interlaminar and intralaminar reinforcement of composite laminates with aligned carbon nanotubes’, *Compos Sci Technol*, vol. 70, no. 1, pp. 20–28, Jan. 2010, doi: 10.1016/j.compscitech.2009.09.001.

[2] E. GARCIA, B. WARDLE, A. JOHNHART, and N. YAMAMOTO, 'Fabrication and multifunctional properties of a hybrid laminate with aligned carbon nanotubes grown In Situ', *Compos Sci Technol*, vol. 68, no. 9, pp. 2034–2041, Jul. 2008, doi: 10.1016/j.compscitech.2008.02.028.

[3] M. R. Maschmann *et al.*, 'Bioinspired Carbon Nanotube Fuzzy Fiber Hair Sensor for Air-Flow Detection', *Advanced Materials*, vol. 26, no. 20, pp. 3230–3234, May 2014, doi: 10.1002/adma.201305285.

[4] M. R. Maschmann, B. Dickinson, G. J. Ehlert, and J. W. Baur, 'Force sensitive carbon nanotube arrays for biologically inspired airflow sensing', *Smart Mater Struct*, vol. 21, no. 9, p. 094024, Sep. 2012, doi: 10.1088/0964-1726/21/9/094024.

[5] A. D. Franklin *et al.*, 'Sub-10 nm Carbon Nanotube Transistor', *Nano Lett*, vol. 12, no. 2, pp. 758–762, Feb. 2012, doi: 10.1021/nl203701g.

[6] B. A. Cola, P. B. Amama, X. Xu, and T. S. Fisher, 'Effects of Growth Temperature on Carbon Nanotube Array Thermal Interfaces', *J Heat Transfer*, vol. 130, no. 11, Nov. 2008, doi: 10.1115/1.2969758.

[7] J. Xu and T. S. Fisher, 'Enhancement of thermal interface materials with carbon nanotube arrays', *Int J Heat Mass Transf*, vol. 49, no. 9–10, pp. 1658–1666, May 2006, doi: 10.1016/j.ijheatmasstransfer.2005.09.039.

[8] B. A. Cola, J. Xu, C. Cheng, X. Xu, T. S. Fisher, and H. Hu, 'Photoacoustic characterization of carbon nanotube array thermal interfaces', *J Appl Phys*, vol. 101, no. 5, p. 054313, Mar. 2007, doi: 10.1063/1.2510998.

[9] M. R. Maschmann, Q. Zhang, F. Du, L. Dai, and J. Baur, 'Length dependent foam-like mechanical response of axially indented vertically oriented carbon nanotube arrays', *Carbon N Y*, vol. 49, no. 2, pp. 386–397, Feb. 2011, doi: 10.1016/j.carbon.2010.09.034.

[10] A. A. Zbib, S. D. Mesarovic, E. T. Lilleodden, D. McClain, J. Jiao, and D. F. Bahr, 'The coordinated buckling of carbon nanotube turfs under uniform compression', *Nanotechnology*, vol. 19, no. 17, p. 175704, Apr. 2008, doi: 10.1088/0957-4484/19/17/175704.

[11] M. R. Maschmann, Q. Zhang, R. Wheeler, F. Du, L. Dai, and J. Baur, 'In situ SEM Observation of Column-like and Foam-like CNT Array Nanoindentation', *ACS Appl Mater Interfaces*, vol. 3, no. 3, pp. 648–653, Mar. 2011, doi: 10.1021/am101262g.

[12] A. Brieland-Shoultz *et al.*, 'Scaling the Stiffness, Strength, and Toughness of Ceramic-Coated Nanotube Foams into the Structural Regime', *Adv Funct Mater*, vol. 24, no. 36, pp. 5728–5735, Sep. 2014, doi: 10.1002/adfm.201400851.

[13] B. F. Davis, X. Yan, N. Muralidharan, L. Oakes, C. L. Pint, and M. R. Maschmann, 'Electrically Conductive Hierarchical Carbon Nanotube Networks with Tunable Mechanical Response', *ACS Appl Mater Interfaces*, vol. 8, no. 41, pp. 28004–28011, Oct. 2016, doi: 10.1021/acsami.6b10726.

[14] S. B. Hutchens, L. J. Hall, and J. R. Greer, 'In situ Mechanical Testing Reveals Periodic Buckle Nucleation and Propagation in Carbon Nanotube Bundles', *Adv Funct Mater*, vol. 20, no. 14, pp. 2338–2346, May 2010, doi: 10.1002/adfm.201000305.

[15] A. Cao, P. L. Dickrell, W. G. Sawyer, M. N. Ghasemi-Nejhad, and P. M. Ajayan, 'Super-Compressible Foamlike Carbon Nanotube Films', *Science (1979)*, vol. 310, no. 5752, pp. 1307–1310, Nov. 2005, doi: 10.1126/science.1118957.

[16] M. R. Maschmann, G. J. Ehlert, S. Tawfick, A. J. Hart, and J. W. Baur, 'Continuum analysis of carbon nanotube array buckling enabled by anisotropic elastic measurements and modeling', *Carbon N Y*, vol. 66, pp. 377–386, Jan. 2014, doi: 10.1016/j.carbon.2013.09.013.

[17] S. Pathak, E. J. Lim, P. Pour Shahid Saeed Abadi, S. Graham, B. A. Cola, and J. R. Greer, 'Higher Recovery and Better Energy Dissipation at Faster Strain Rates in Carbon Nanotube Bundles: An *in-Situ* Study', *ACS Nano*, vol. 6, no. 3, pp. 2189–2197, Mar. 2012, doi: 10.1021/nn300376j.

[18] P. B. Amama *et al.*, 'Influence of Alumina Type on the Evolution and Activity of Alumina-Supported Fe Catalysts in Single-Walled Carbon Nanotube Carpet Growth', *ACS Nano*, vol. 4, no. 2, pp. 895–904, Feb. 2010, doi: 10.1021/nn901700u.

[19] S. W. Pattinson *et al.*, 'In Situ Observation of the Effect of Nitrogen on Carbon Nanotube Synthesis', *Chemistry of Materials*, vol. 25, no. 15, pp. 2921–2923, Aug. 2013, doi: 10.1021/cm401216q.

[20] V. Balakrishnan *et al.*, 'Real-Time Imaging of Self-Organization and Mechanical Competition in Carbon Nanotube Forest Growth', *ACS Nano*, vol. 10, no. 12, pp. 11496–11504, Dec. 2016, doi: 10.1021/acsnano.6b07251.

[21] A. Yasuda, N. Kawase, and W. Mizutani, 'Carbon-Nanotube Formation Mechanism Based on in Situ TEM Observations', *J Phys Chem B*, vol. 106, no. 51, pp. 13294–13298, Dec. 2002, doi: 10.1021/jp020977l.

[22] M. Bedewy, B. Viswanath, E. R. Meshot, D. N. Zakharov, E. A. Stach, and A. J. Hart, 'Measurement of the Dewetting, Nucleation, and Deactivation Kinetics of Carbon Nanotube Population Growth by Environmental Transmission Electron Microscopy', *Chemistry of Materials*, vol. 28, no. 11, pp. 3804–3813, Jun. 2016, doi: 10.1021/acs.chemmater.6b00798.

[23] N. T. Dee *et al.*, 'Carbon-assisted catalyst pretreatment enables straightforward synthesis of high-density carbon nanotube forests', *Carbon N Y*, vol. 153, pp. 196–205, Nov. 2019, doi: 10.1016/j.carbon.2019.06.083.

[24] X. Huang, R. Farra, R. Schlögl, and M.-G. Willinger, 'Growth and Termination Dynamics of Multiwalled Carbon Nanotubes at Near Ambient Pressure: An in Situ Transmission Electron Microscopy Study', *Nano Lett*,

vol. 19, no. 8, pp. 5380–5387, Aug. 2019, doi: 10.1021/acs.nanolett.9b01888.

[25] A. P. Graham *et al.*, 'How do carbon nanotubes fit into the semiconductor roadmap?', *Applied Physics A*, vol. 80, no. 6, pp. 1141–1151, Mar. 2005, doi: 10.1007/s00339-004-3151-7.

[26] H. Dai, E. W. Wong, and C. M. Lieber, 'Probing Electrical Transport in Nanomaterials: Conductivity of Individual Carbon Nanotubes', *Science (1979)*, vol. 272, no. 5261, pp. 523–526, Apr. 1996, doi: 10.1126/science.272.5261.523.

[27] B. Q. Wei, R. Vajtai, and P. M. Ajayan, 'Reliability and current carrying capacity of carbon nanotubes', *Appl Phys Lett*, vol. 79, no. 8, pp. 1172–1174, Aug. 2001, doi: 10.1063/1.1396632.

[28] C. Li, E. T. Thostenson, and T.-W. Chou, 'Dominant role of tunneling resistance in the electrical conductivity of carbon nanotube–based composites', *Appl Phys Lett*, vol. 91, no. 22, p. 223114, Nov. 2007, doi: 10.1063/1.2819690.

[29] W. Bauhofer and J. Z. Kovacs, 'A review and analysis of electrical percolation in carbon nanotube polymer composites', *Compos Sci Technol*, vol. 69, no. 10, pp. 1486–1498, Aug. 2009, doi: 10.1016/j.compscitech.2008.06.018.

[30] R. Rao, D. Liptak, T. Cherukuri, B. I. Yakobson, and B. Maruyama, 'In situ evidence for chirality-dependent growth rates of individual carbon nanotubes', *Nat Mater*, vol. 11, no. 3, pp. 213–216, Mar. 2012, doi: 10.1038/nmat3231.

[31] P. Nikolaev *et al.*, 'Autonomy in materials research: a case study in carbon nanotube growth', *NPJ Comput Mater*, vol. 2, no. 1, p. 16031, Oct. 2016, doi: 10.1038/npjcompumats.2016.31.

[32] T. Hajilounezhad and M. R. Maschmann, 'Numerical Investigation of Internal Forces During Carbon Nanotube Forest Self-Assembly', in *Volume 2: Advanced Manufacturing*, American Society of Mechanical Engineers, Nov. 2018. doi: 10.1115/IMECE2018-86567.

[33] M. R. Maschmann, 'Integrated simulation of active carbon nanotube forest growth and mechanical compression', *Carbon N Y*, vol. 86, pp. 26–37, May 2015, doi: 10.1016/j.carbon.2015.01.013.

[34] T. Hajilounezhad, D. M. Ajiboye, and M. R. Maschmann, 'Evaluating the forces generated during carbon nanotube forest growth and self-assembly', *Materialia (Oxf)*, vol. 7, p. 100371, Sep. 2019, doi: 10.1016/j.mtla.2019.100371.

[35] T. Hajilounezhad, R. Bao, K. Palaniappan, F. Bunyak, P. Calyam, and M. R. Maschmann, 'Predicting carbon nanotube forest attributes and mechanical properties using simulated images and deep learning', *NPJ Comput Mater*, vol. 7, no. 1, p. 134, Aug. 2021, doi: 10.1038/s41524-021-00603-8.

[36] 'Fusion Brochure http://protochips.com/wp-content/uploads/2017/10/Fusion-Brochure.pdf. '.

[37] G. Koerner, R. Surya, and M. Maschmann, 'CNT Forest Self-Assembly Insights from In-situ SEM Synthesis [in review]'.

[38] G. Koerner, R. Surya, K. Palaniappan, P. Calyam, F. Bunyak, and M. R. Maschmann, 'In-Situ Scanning Electron Microscope Chemical Vapor Deposition as a Platform for Nanomanufacturing Insights', in *Volume 2B: Advanced Manufacturing*, American Society of Mechanical Engineers, Nov. 2021. doi: 10.1115/IMECE2021-73554.

[39] J. Schindelin *et al.*, 'Fiji: an open-source platform for biological-image analysis', *Nat Methods*, vol. 9, no. 7, pp. 676–682, Jul. 2012, doi: 10.1038/nmeth.2019.